Ferroelectric Fluids for Nonlinear Photonics: Evaluation of Temperature Dependence of Second-Order Susceptibilities

Matija Lovšin, Luka Cmok, Calum J. Gibb, Jordan Hobbs, Richard J. Mandle, Alenka Mertelj, Irena Drevenšek-Olenik, and Nerea Sebastián**

Ferroelectric nematic fluids are promising materials for tunable nonlinear photonics, with applications ranging from second harmonic generation to sources of entangled photons. However, the few reported values of second-order susceptibilities vary widely depending on the molecular architecture. Here, we systematically measure second-order NLO susceptibilities of five different materials that exhibit the ferroelectric nematic phase, as well as the more recently discovered layered smectic A ferroelectric phase. The materials investigated include archetypal molecular architectures as well as mixtures showing room-temperature ferroelectric phases. The measured values, which range from 0.3 to 20 pm V^{-1}, are here reasonably predicted by combining calculations of molecular-level hyperpolarizabilities and a simple nematic potential, highlighting the opportunities of modelling-assisted design for enhanced NLO ferroelectric fluids.

1. Introduction

Nonlinear optical (NLO) materials play a crucial role in a wide range of applications, from frequency conversion to laser systems, telecommunications, and even quantum technologies.[1–3] Historically, commercial NLO components have relied on solid-state crystals,[4] like lithium niobate (LN), potassium dihydrogen phosphate (KDP), potassium titanyl phosphate (KTP), and barium borate (BBO), which all exhibit good NLO properties yet lack the tunability and flexibility of soft matter materials.

A new alternative emerged in 2017 with the discovery of the first two ferroelectric nematic liquid crystalline (FNLC) materials, RM734 and DIO.[5–9] These materials exhibit a nematic liquid crystal phase with a macroscopic electric polarization: the ferroelectric nematic (N_F) phase. Their polar order breaks the inversion symmetry, enabling second-order NLO processes, like optical second harmonic generation (SHG), to emerge. To achieve efficient SHG, two material properties are important: large NLO susceptibility coefficients and the possibility to attain material orientation/configuration that leads to phase matching. The second-order NLO susceptibility is the third-order tensor that connects the second-order electric polarization to the electric field: $P = \epsilon_0\ \chi^{(2)} : E\ \ E$. By convention, the following NLO tensor is introduced: $\mathrm{d}_{\mathrm{ijk}} = \frac{1}{2}\ \chi^{2}_{\mathrm{ijk}}$. Considering permutation symmetries, the last 2 indices can be replaced by one, resulting in a second-order tensor with 18 components: $d_{ijk} d_{il}$. The first measurements of the NLO coefficients report the values d_{33} = 5.6 pm V^{-1} for RM734[10] and d_{33} = 0.24 pm V^{-1} for DIO.[11] Although these values are about one order of magnitude lower than those of traditional NLO crystals (e.g., LN: d_{33} = 25.7 pm V^{-1}[12]) and on par with quartz (d_{11} = 0.3 pm V^{-1}[12]), targeted molecular design focused on enhancing hyperpolarizability along the donor-acceptor axis may possibly lead to even surpassing them. For instance, adding chromophores to RM734 led to an increase in the d_{33} up to 25 pm V^{-1} [13] in the absorption regime. Another material requirement for the efficient SHG process is the possibility to obtain phase matching between the fundamental and the second harmonic optical waves. In this respect, FNLCs provide several new options. For instance, conversion efficiency can be significantly increased by introducing chiral dopants that induce a periodic helielectric nematic structure and subsequently enable quasi-phase matching conditions to be realized.[14–18]

Still, the greatest advantage of FNLCs against NLO crystals is in novel capabilities to control the material orientation and

---

M. Lovšin, L. Cmok, A. Mertelj, I. Drevenšek-Olenik, N. Sebastián
Department of Complex Matter
Jožef Stefan Institute
Ljubljana 1000, Slovenia
E-mail: matija.lovsin@ijs.si; nerea.sebastian@ijs.si

M. Lovšin, L. Cmok, I. Drevenšek-Olenik
Faculty of Mathematics and Physics
University of Ljubljana
Ljubljana 1000, Slovenia

L. Cmok
CENN Nanocenter
Ljubljana 1000, Slovenia

C. J. Gibb, R. J. Mandle
School of Chemistry
University of Leeds
Leeds LS2 9JT, UK

J. Hobbs, R. J. Mandle
School of Physics and Astronomy
University of Leeds
Leeds LS2 9JT, UK

The ORCID identification number(s) for the author(s) of this article can be found under https://doi.org/10.1002/adom.202503018

DOI: 10.1002/adom.202503018

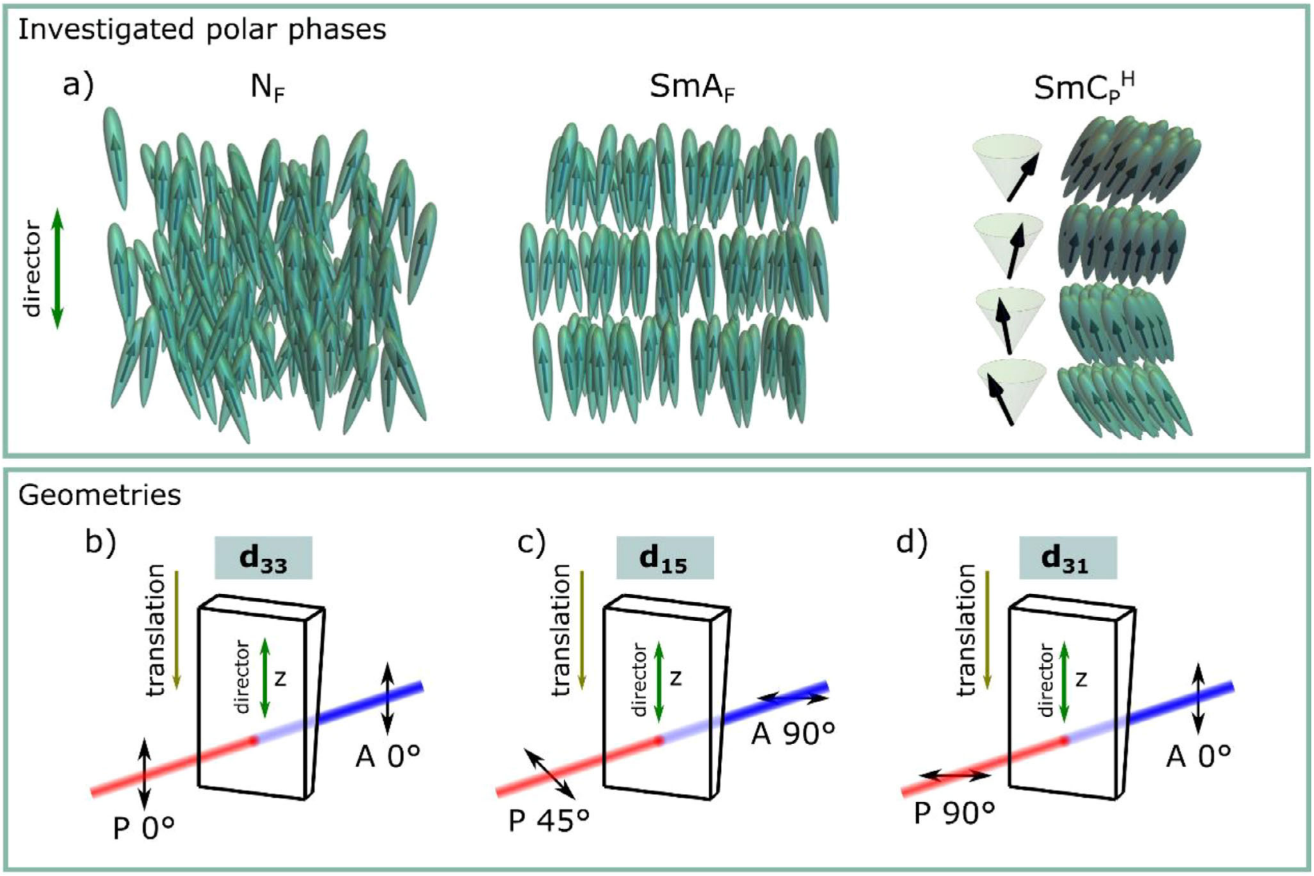

Figure 1. a) Sketch of the polar mesophases investigated in this work, from left to right: ferroelectric nematic phase (NF), ferroelectric smectic A phase (SmAF) and polar heliconical smectic C phase (SmCPH) SHG. b-c) Considering the $C_{\infty v}$ symmetry of the studied phases, the number of independent nonzero components of the NLO susceptibility tensor is 3 (d_{33}, d_{15}, and d_{31}) which are measured in the geometries depicted here showing the polarization of the fundamental beam and analyzer relative to the director (green arrow) and wedge geometry for b) d_{33}, c) d_{15}, and d) d_{31}.

therefore its effective NLO response by various passive as well as active methods. It has been shown that targeted surface alignment allows control of the polarization direction[19–23] and enables the creation of 1D and 2D SHG patterns on a micrometer scale.[19,24] Another strategy is to actuate the FNLC orientation using external electric fields,[25] which leads to strong modulation of the SHG signal.

The discovery of the ferroelectric nematic phase (N_F, **Figure 1a**) was followed by the discovery of many new polar phases, combining both orientational and positional order. Interesting for the NLO applications, is the polar smectic phase (SmA_F, Figure 1a),[26–28] in which molecules are layered with their long axes on average perpendicular to the layers, while exhibiting ferroelectric ordering of the molecular dipoles (Figure 1a). More recently, spontaneous chiral symmetry breaking in these polar fluids was reported, giving rise to the ferroelectric twist-bent nematic phase (N_{TBF}),[29–31] and polar chiral tilted smectic phase ($SmC_P{}^H$, Figure 1a).[26] Introduction of molecular chirality, not only transforms the N_F phase into its helical analogue $N_F{}^*$,[32] but leads to more complex structural arrangements, such as and twist-grain boundary phases.[33]

Although the initial assessment of the SHG properties of RM734 and DIO has been conducted, the thorough characterization of the nonlinear susceptibility tensor coefficients (d_{ij}) and systematic measurements of dispersion of refractive indices are needed before planning any NLO components. In this work, we employ the Maker fringes method to perform the first temperature dependence analysis of the d_{ij} coefficients for several materials exhibiting a variety of polar phases. We first analyse NLO components in the N_F phase of RM734 and DIO, which exhibit on cooling the phase sequence N-N_S-N_F, being N_S phase a modulated antiferroelectric phase, whose structure is still being discussed and also referred to as N_x/M2/SmZ_A.[5,34] We additionally determine the d_{ij} coefficients in the polar SmA_F and $SmC_P{}^H$ phases (Figure 1a) of a recently reported material, C1,[26] and perform the comparative analysis between the pure compounds and a binary mixture of DIO and C1 (F7), showing the N_F phase down to room temperature. Finally, we additionally investigate the nonlinear susceptibility tensor coefficients for FNLC-1571, a room temperature N_F mixture provided by Merck Electronics. The molecular structures together with the complete phase sequence of the investigated materials are shown in Figure S1 (Supporting Information). In the end, we benchmarked our findings against a combined experimental and computational method that could guide the design of new polar liquid crystals with optimal NLO properties.

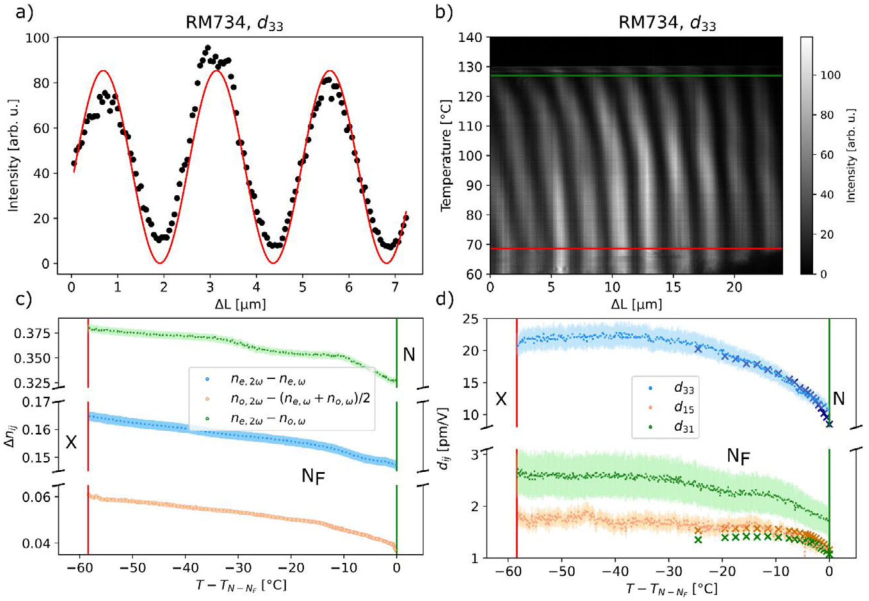

Figure 2. Second-order susceptibility measurement of RM734. a) SHG intensity as a function of cell thickness variation for RM734 at 102 °C corresponding to the measurement of d_{33}. Profile was obtained at each temperature by averaging the intensity along the fringes over 90 pixels. Red lines correspond to the fit to Equation (10). b) Reconstructed temperature dependence of the SHG intensity profiles (a) corresponding to the d_{33} geometry, illustrating the evolution of the Maker's fringes across the N_F phase range. c) The measured refractive index mismatch Δn_{ij} and d) the corresponding NLO susceptibility components d_{33}, d_{15}, and d_{31} of RM734. The measured data (dots) with their uncertainties (shaded area) compared to the values calculated from molecular hyperpolarizability (crosses). The first SHG signal was detected at 130.5 °C, and the N_F phase stabilized at 127 °C (green line). The SHG signal disappeared at 68.6 °C upon crystallization (X) (red line).

2. Results

We measured d_{ij} coefficients using Maker fringes method and employing wedge cells of varying thickness with different slopes (dihedral angle ranging from 1.27° to 0.07°) and with surface coating promoting in-plane alignment of the director along the wedge direction. In the wedge Makers Fringes method, the optical power of the second harmonic beam varies periodically with thickness (L) as described in depth in Methods and, from the periodic oscillations, it is possible to determine the dispersion of the involved refractive indexes for a given process (Δn_{ij}) and the corresponding d_{ij} coefficient can be determined from the maximum intensity detected in a calibrated setup (see Experimental Section and Figure S2, Supporting Information). In the majority of the cases, cells with large slope were used, allowing for direct imaging of the Maker's Fringes (e.g., in Figure S8, Supporting Information) with a CMOS camera within the laser beam spot size. In the case of DIO, a custom-made cell had to be employed with smaller slope and measurements were performed by translating the cell along the wedge direction (Figure 1b–d).

The considered LC phases N_F and SmA_F have $C_{\infty v}$ symmetry, and the symmetry of the $SmC_P{}^H$ can be treated as $C_{\infty v}$ as well, because the period of the helical structure is much smaller than the optical wavelengths. Consequently, the number of independent nonzero components of the NLO susceptibility for all the investigated LC phases reduces to 3:

$$d = \begin{pmatrix} 0 & 0 & 0 & 0 & d_{15} & 0 \\ 0 & 0 & 0 & d_{15} & 0 & 0 \\ d_{31} & d_{31} & d_{33} & 0 & 0 & 0 \end{pmatrix} \tag{1}$$

where the z-axis is along the director. According to Kleinman symmetry, in the absence of dispersion and absorption in the medium, the d_{31} should be equal to d_{15}, reducing the number of distinct components to 2. However, liquid crystals are dispersive materials, and the components remain distinct, although their values are expected to be similar. To measure a specific component of the nonlinear susceptibility tensor dij, the orientation of the fundamental beam polarization and the analyzer for the second harmonic beam were set as shown in Figure 1b–d, i.e., d_{33} corresponds to both incoming fundamental beam and SH signal being polarized along the director; d_{15} corresponds to incoming polarization inclined at 45° to the director and detecting SH signal perpendicular to the director; d_{31} corresponds to incoming polarization perpendicular to the director and detecting SH signal along the director.

The first material we measured was RM734. It aligned well in the commercial wedge cell, which has a sufficient slope to allow for the imaging of multiple Maker fringes within the beam spot (Figure S8, Supporting Information). In order to determine all three components of the nonlinear susceptibility tensor, the three geometries described in the Figure 1 were explored. For each image, the intensity was averaged over several pixels along the fringes to obtain the Maker's Fringes profiles shown in **Figure 2**a. At each temperature the same area was analysed, yielding a series of Maker's Fringes profiles, which are plotted versus temperature in Figure 2b to showcase their evolution. Each fringes profile was then fitted to Equation (10), from which the refractive index mismatch as a function of temperature (Figure 2c) and the temperature dependence of the d_{ij} coefficients can be obtained (Figure 2d). The component with the largest value was d_{33}, which,

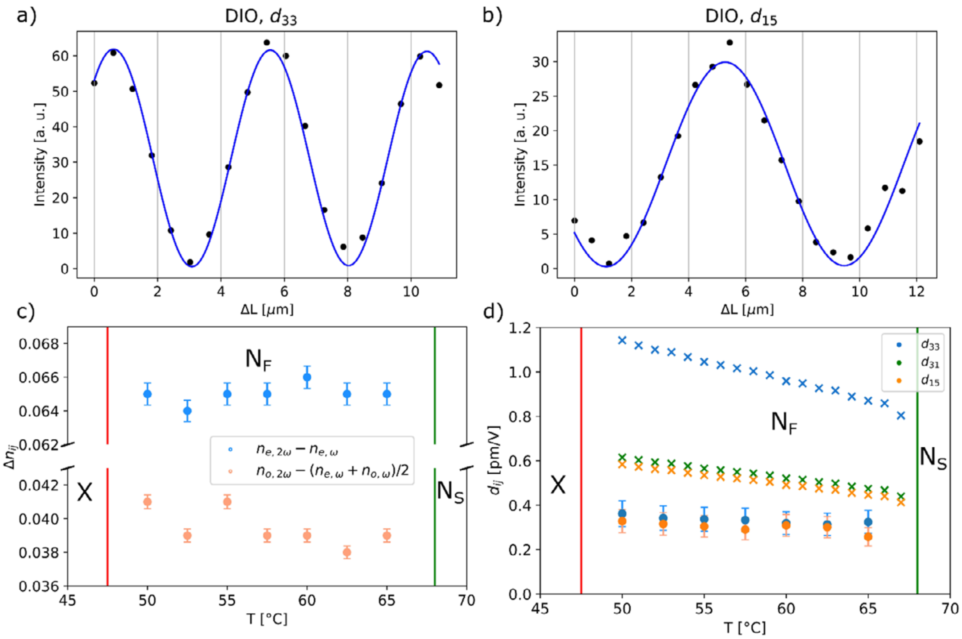

Figure 3. Second-order susceptibility measurement of DIO. SHG intensity as a function of cell thickness for DIO at 65 °C (the measurement of a) d_{33} and b) d_{15}). Blue lines correspond to the fit to Equation (10). c) The measured refractive index mismatch Δn and d) the corresponding NLO susceptibility components d_{33} and d_{15} of DIO. The measured data (dots) with their error bars compared to the values calculated from molecular hyperpolarizability (crosses). The phase transition N_S-N_F occurred at 68 °C (green line), and the SHG signal disappeared at 47.5 °C (red line).

with decreasing temperature, increased in value up to 22.5 ± 2 pm/V.

The maximum measured value of d_{15} of RM734 is an order of magnitude lower than d_{33}, reaching $d_{15} = 1.8 \pm 0.2$ pm/V. For all measured materials, the refractive index mismatch $\Delta n_{31} = n_{e,2\omega} - n_{o,\omega}$ is expected to be significantly larger than $\Delta n_{15} = n_{o,2\omega} - (n_{e,\omega} + n_{o,\omega})/2$ (n_e denotes the extraordinary refractive index, oriented along the director, and n_o the ordinary refractive index, oriented perpendicular to the director). Consequently, as the SHG intensity is inversely proportional to Δn^2 (Equation 9), it follows that even when d_{31} is comparable to d_{15}, the amplitude of the Maker fringes associated with d_{31} is much lower, making this component more difficult to measure. This is an issue that will also appear and affect the rest of the studied materials. In our analysis, RM734 was the only material for which the d_{31} component could be measured. For all other measured materials, the maximum signal in the measurements of d_{31} was too low to be acquired with the current setup.

We then checked DIO, for which there is also some published data on the NLO susceptibility.[11] DIO did not align well in the commercial cell, and a custom-made cell was needed. This cell has a lower wedge slope ($\alpha = 0.07°$), and it had to be translated along the wedge in order to detect enough Maker fringes. We were able to measure the d_{33} and d_{15} components (**Figure 3**), but not the d_{31}. The reason for this could be the small period of the Maker fringes, the larger expected value for Δn_{31} in combination with a small NLO coefficient, as both of those cause a low maximum SHG signal of the fringes. Signal could be enhanced by higher fundamental beam power; however, this approach is limited by sample degradation and thermal effects, and thus, was discarded. The obtained values of both d_{33} and d_{15} are similar to each other and much lower than those of RM734, ≈0.35 pm V^{-1}. In the Supporting Information of,[19] it was already shown that, in contrast to RM734, in DIO, the d_{15} component significantly contributes to the net SHG signal. The authors reported that the SHG signal was stronger when the pump beam polarization was at 45° with respect to the director than when it was parallel to it, which indicates that the cell thickness used in their experiment was closer to the Maker minimum for d_{33} than for d_{15}. DIO is a fundamental part of material F7, which also contains C1.

The polar smectic material C1 was measured both in the SmA_F and the $SmC_P{}^H$ phases and results are shown in **Figure 4**. The maximal measured values of d_{33} and d_{15} in the SmA_F phase are $d_{33} = 3.9 \pm 0.6$ pm/V and $d_{15} = 0.35 \pm 0.06$ pm/V at 88 °C, which is the temperature of the phase transition to $SmC_P{}^H$. The gap in Figure 4 corresponds to the range of temperatures during $SmA_F - SmC_P{}^H$ phase transition, in which the $SmC_P{}^H$ phase has not stabilized yet. As mentioned earlier, since the helical pitch is much smaller than the optical wavelengths, the symmetry of the $SmC_P{}^H$ phase can be treated as $C_{\infty v}$. The effective values of d_{33} and d_{15} are somewhat smaller than before the transition, and they decrease with cooling. As in DIO, also in C1, the d_{31} component could not be measured because the SHG signal was too low.

The last two materials that we investigated are especially promising for the NLO applications, given that they exhibit the N_F phase at room temperature. For the material F7, which is a mixture of 30% C1 and 70% DIO, we expected values of the d_{ij} between those measured for the pure materials. The obtained peak values are $d_{33} = 2.1 \pm 0.2$ pm V and $d_{15} = 0.47 \pm 0.07$ pm/V

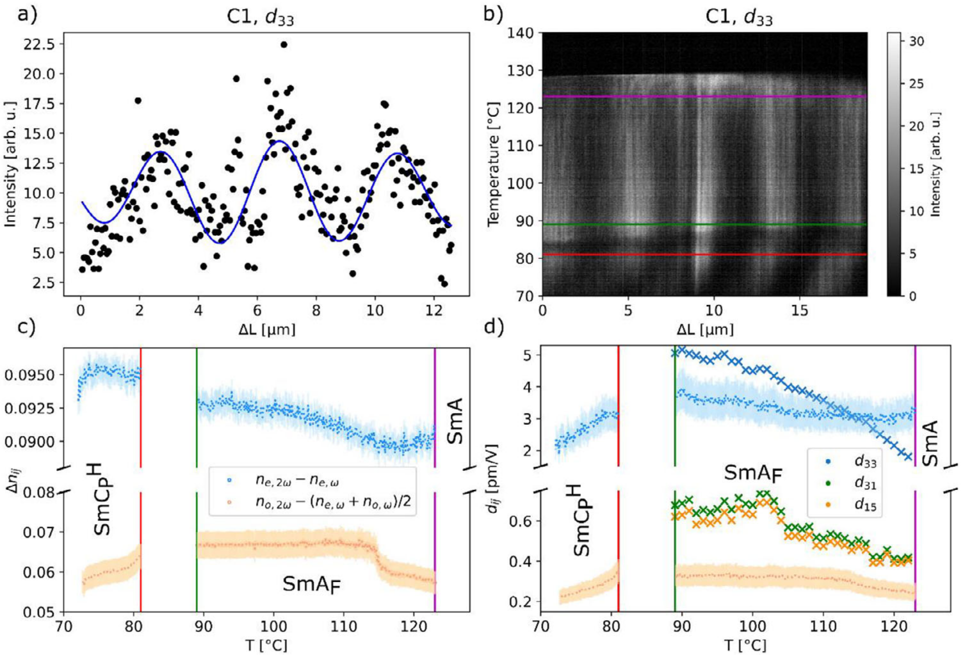

Figure 4. Second-order susceptibility measurement of C1. a) SHG intensity as a function of cell thickness variation for C1 at 119 °C corresponding to the measurement of d_{33}. Profile was obtained at each temperature by averaging the intensity along the fringes over 40 pixels. Red lines correspond to the fit to Equation (10). b) Reconstructed temperature dependence of the SHG intensity profiles (a) corresponding to the d_{33} geometry, illustrating the evolution of the Maker's fringes across the N_F phase range. c) The measured refractive index mismatch Δn and d) the corresponding NLO susceptibility components d_{33} and d_{15} of C1. The measured data (dots) with their uncertainties (shaded area) compared to the values calculated from molecular hyperpolarizability (crosses). The phase transition SmA-SmA$_F$ of C1 occurred at 123 °C (magenta line), the phase transition to SmC$_P$^{H} started at 89 °C (green line), and the SmC$_P$^{H} phase stabilized at 81 °C (red line).

(**Figure 5**), while the weighted average of C1 and DIO would be $d_{33} = 1.4$ pm/V and $d_{15} = 0.33$ pm/V. As in previous cases, the signal of the d_{31} was too low to be measured.

The last investigated material, ferroelectric nematic material FNLC-1571, exhibits the N_F phase at room temperature as well and is now widely used as a study material. In a previous study, a value of $d_{33} \approx 20$ pm V^{-1} has been reported for $\lambda = 1370$ nm, determined by a measurement using single sample thickness and compared with that of a reference sample.[35] As the FNLC-1571 did not align well in the commercial cell, we used two different custom-made wedge cells, one with a wedge slope $\alpha = 1.27°$ and one with a wedge slope $\alpha = 0.07°$, with the result of the latter allowing us to associate the non-zero signal of fringes' minima (**Figure 6a**; Figure S11, Supporting Information) to the large wedge slope of the former. A representative example of the Maker's fringes, its analysis and the temperature dependence for the different coefficients and involved dispersions on heating is shown in Figure 6. The measurements of d_{33} and d_{15} show weak temperature dependence (for d_{33} from 9 to 11 pm V^{-1} and for $d_{15} \approx 0.45$ pm V^{-1}). A slight difference in the transition temperature into the higher temperature antiferroelectric phase between the measurements of d_{33} and d_{15} was detected, most probably provoked by the increased laser power and consequent cell heating, in the d_{15} measurements performed without the Fabry-Pérot filter. Unfortunately, no signal for d_{31} was observed, which could be attributed to a large refractive index mismatch. However, as for the rest of the materials, it is expected to have a similar value to d_{15}.

3. Discussion

We have measured the NLO susceptibility of several materials (**Table 1**), and the results show that they vary significantly from one material to another (from $d_{33} = 0.36 \pm 0.05$ pm/V in DIO to $d_{33} = 22.5 \pm 2$ pm/V in RM734). The difference stems from their molecular structure, highlighting the challenge of designing new molecular structures that will result in optimal NLO properties while preserving the N_F phase. While a comprehensive relationship between NLO properties and molecular structure is outside the scope of this work, due to the limited number of materials available for study, the large NLO susceptibility of RM734 stems from the push-pull system established by the 2,4-dimethoxybenzoate (donor) and 4-nitrophenyl (acceptor) structure. For DIO, C1, and F7, the donor (5-propyl-1,3-dioxane) and acceptor (3,4,5-trifluorobenzene) are far weaker, manifesting in smaller NLO susceptibilities. In the case of C1 the difluoromethyleneoxy group (–O-CF$_2$–) bridge contributes to the enhancement of the push-pull electronic polarization, giving a comparatively larger hyperpolarizabilities for C1 compared to DIO. With the growing number of molecules exhibiting polar phases being designed, it would be beneficial to be able to calculate their potential NLO susceptibility values. To achieve this, it is necessary to relate the measured NLO susceptibility to the molecular properties of the analyzed materials. The macroscopic susceptibility tensor can be related to the microscopic first hyperpolarizabilities considering the oriented gas model, which assumes a collection of molecules whose orientations are specified

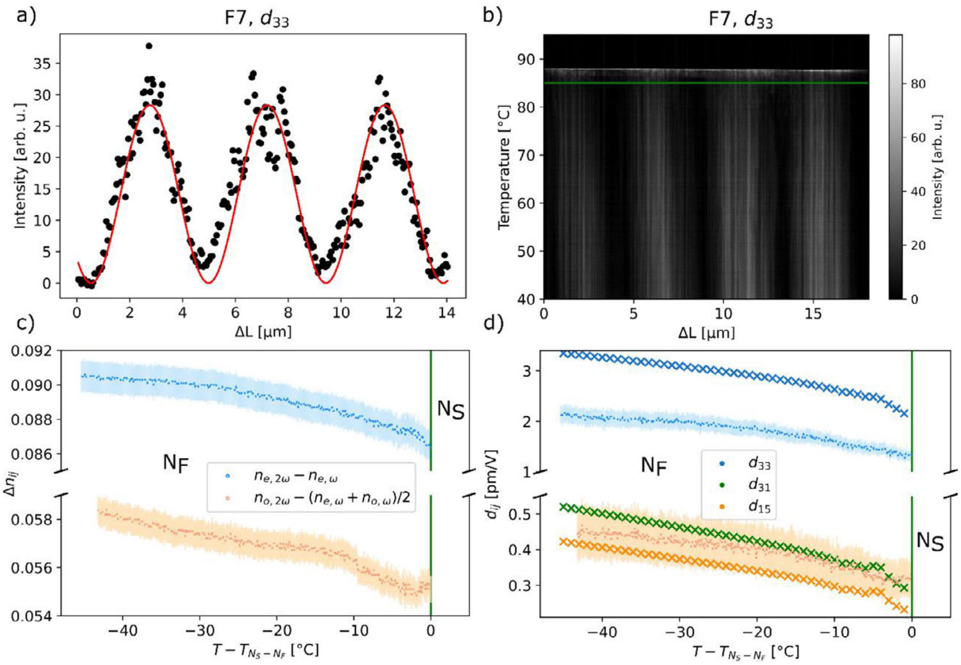

Figure 5. Second-order susceptibility measurement of F7. a) SHG intensity as a function of cell thickness variation for F7 at 55 °C corresponding to the measurement of d_{33}. Profile was obtained at each temperature by averaging the intensity along the fringes over 94 pixels. Red lines correspond to the fit to Equation (10). b) Reconstructed temperature dependence of the SHG intensity profiles (a) corresponding to the d_{33} geometry, illustrating the evolution of the Maker's fringes across the N_F phase range. c) The measured refractive index mismatch Δn and d) the corresponding NLO susceptibility components d_{33} and d_{15} of F7. The measured data (dots) with their uncertainties (shaded area) compared to the values calculated from molecular hyperpolarizability (crosses). The phase transition N_S-N_F of F7 occurred at 85 °C (green line).

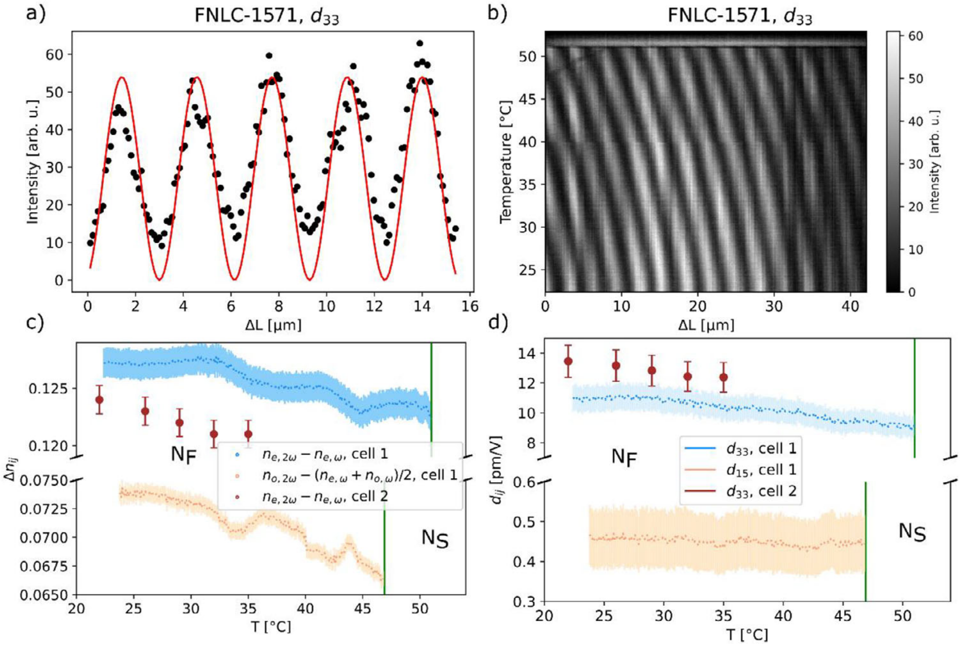

Figure 6. Second-order susceptibility measurement of FNLC-1571. a) SHG intensity as a function of cell thickness variation for FNLC-1571 at 22.3 °C corresponding to the measurement of d_{33}. Profile was obtained at each temperature by averaging the intensity along the fringes over 76 pixels. Red lines correspond to the fit to Equation (10). b) Reconstructed temperature dependence of the SHG intensity profiles (a) corresponding to the d_{33} geometry, illustrating the evolution of the Maker's fringes across the N_F phase range. c) The measured refractive index mismatch Δn and d) the corresponding NLO susceptibility components d_{33} and d_{15} of FNLC-1571. The measured data (dots) with their uncertainties (shaded area). Cell 1 was the cell with a wedge slope of $\alpha = 1.27°$where the Maker fringes could be analyzed from the image, while cell 2 was the cell with a smaller wedge slope of $\alpha = 0.07°$ that had to be translated for each measurement. The phase transition N_F-N_S of FNLC-1571 occurred at 51 °C during the measurement of d_{33} and at 46.8 °C during the measurement of d_{15} (green line).

Table 1. Maximal values of measured second-order NLO susceptibility components.

	RM734 [N_F, 93 °C]	DIO [N_F, 47 °C]	FNLC-1571 [N_F, 23 °C]	C1 [SmA_F, 88 °C]	F7 [N_F, 40 °C]
d_{33} [pm/V]	22.5 ± 2	0.36 ± 0.05	11.0 ± 0.9	3.9 ± 0.6	2.1 ± 0.2
d_{15} [pm/V]	1.8 ± 0.2	0.32 ± 0.05	0.46 ± 0.07	0.35 ± 0.06	0.47 ± 0.07
d_{31} [pm/V]	2.7 ± 0.4				

by a known distribution function. Intermolecular interactions at optical frequencies are incorporated through local-field corrections accounting for the difference between the externally applied macroscopic electric field and the microscopic field experienced by each molecule, and thus, the NLO tensor components can be expressed as:[10]

$$d_{ijk} = N F_{\omega} F_{\omega} F_{2\omega} \left\langle \beta_{ijk} \right\rangle \tag{2}$$

where N is the volume density of the material, $N = \frac{N_A \rho}{M}$, N_A is Avogadro's constant, ρ is density, and M is the molar mass of the material. F_α are the local field factors for the fundamental and the second harmonic frequencies, and $\langle \beta_{ijk} \rangle$ is the thermally averaged first molecular hyperpolarizability.

The local field factor is given by:

$$F\ (\omega) = \frac{n^2 + 2}{3} \tag{3}$$

Usually, it is calculated by taking the average $n = \frac{1}{3}\ (2n_{o,\omega} + n_{e,\omega})$. Considering dispersion, and calculating for each refractive index separately, results in ≈20% higher local field correction factor in our case (Figure S9, Supporting Information). Additional improvement of the local field factor calculation accuracy can be done if the uniaxial liquid crystals are treated as anisotropic crystals with a tetragonal lattice approximation:[36]

$$\begin{aligned} F\ \left(\omega_e\right) &= 1 - L_{ee} \left(n_e^2 - 1\right) \\ F\ \left(\omega_o\right) &= 1 - L_{oo} \left(n_o^2 - 1\right) \end{aligned} \tag{4}$$

where L_{ee} and L_{oo} are the diagonal components of the Lorentz factor tensor, which depend on the degree of anisotropy. As the tensor is traceless, the relation between its components is $L_{oo} = \frac{1}{2}\ (1 - L_{ee})$. The L_{ee} was determined to be between 0.2 and 0.28 for a few typical nematic liquid crystals.[37] We assume the FNLCs to be in the same order of magnitude.

Another way to describe the local field factor has been proposed to introduce anisotropy in the model for isotropic liquids:[38]

$$\begin{aligned} F\ \left(\omega_e\right) &= \tfrac{n_e^2+2}{3} + \eta_{ee} \left(n_e^2 - 1\right) \\ F\ \left(\omega_o\right) &= \tfrac{n_o^2+2}{3} + \eta_{oo} \left(n_o^2 - 1\right) \end{aligned} \tag{5}$$

where η_{ee} and η_{oo} are components of the anisotropy tensor that depend on the pair distribution function. The values for a typical nematic liquid crystal were determined to be between 0.06 and 0.08.[38]

To assess the effect of correction, we plot the local field factor dependence on the level of anisotropy (Figure S8, Supporting Information). We see that the values of F(ω) calculated in this way are lower, and the calculation with the average $n = \frac{1}{3}\ (2n_{o,\omega} + n_{e,\omega})$ gives us a good approximation in the highlighted grey area.

For calculating the thermally averaged first molecular hyperpolarizability $\langle \beta_{ijk} \rangle$, the corresponding thermal averages for the polar angle are needed. They can be calculated from the nematic potential, which was take as proposed in Folcia et al.:[10]

$$U\ (\theta) = A\,(T) \sin^2\theta + B\,(T) \sin^2\frac{\theta}{2} \tag{6}$$

where θ is the polar angle and parameters $A(T)$ and $B(T)$ account for the usual nematic potential and the new contribution due to polarity, and can be calculated from the measured data of polarization and birefringence of the material:

$$\langle \cos\theta \rangle = \frac{P\,(T)}{N\mu} \tag{7}$$

and

$$\frac{S}{S_{NP}} = \frac{\Delta n}{\Delta n_{NP}} \tag{8}$$

where $P(T)$ is the spontaneous polarization of the material, μ is the dipole moment of the molecule, and S_{NP} and Δn_{NP} are the extrapolated order parameter and the birefringence in the case of $B\,(T) =\ 0$ (standard nematic phase). The values of Δn_{NP} can be obtained by extrapolating the birefringence of the N phase into the N_F phase temperature range. As the birefringence in the SmA phase mainly comes from the orientational order, not from the translational one, Equations (6–8) can also be applied for the SmA–SmA_F phase transition in C1. As the dipole moment μ is not parallel to the molecular long axis, only its component along the long axis was considered in the calculations. All other data used for calculations are presented in Table S4 (Supporting Information).

The thermally averaged hyperpolarizability components in the laboratory frame $\langle \beta_{ijk} \rangle$ were calculated from the ones in the molecular frame according to Equations S1–S3 (Supporting Information).[39,40] The components of the hyperpolarizability tensor in the molecular frame were obtained by performing density functional theory (DFT) calculations of the molecular electronic structure with the Gaussian software package at the M06HF-D3/aug-cc-pVTZ level at the optical frequency corresponding to an optical wavelength of 800 nm. Values thus obtained are given in Tables S1–S3 (Supporting Information). However, it should be noted here that Gaussian calculations are for a single molecular conformation and thus limit the accuracy of the results.

As a case example, we start with RM734, for which the polarization data were taken from[8] and the measured birefringence at 405 nm is shown in Figure S9 (Supporting Information). The calculated NLO tensor components are shown in Figure 2 together with the experimental data, showing a very good match with the measurements for d_{33} and d_{15}, while a slightly worse match for d_{31}, likely due to the fact that d_{31} was measured without the Fabry-Pérot filter. However, it is worth recalling here that several approximations are needed for these calculations, especially in regards of local fields and that molecular hyperpolarizability values are calculated only for a given conformation, so even a larger mismatch for any of the components would have been a positive result and although the good agreement for RM734 is encouraging, it should not be overinterpreted.

We compare our results with the only available data for d_{33} of RM734 at a single temperature.[10] For that, we follow their procedure of calculating the hyperpolarizability tensor only from the reported measured values for the NO_2-π-O group and use the fundamental wavelength of 800 nm (as opposed to 1064 nm in their measurement). In their case, the hyperpolarizability is calculated with the two-level dispersion model, assuming the resonance wavelength at $\lambda_{max} = 304$ nm and data from:[41] $\beta_{1907nm} = 3.0 \times 10^{-30}$ esu, leading to: $\beta_{1064nm} = 4.2 \times 10^{-30}$ esu and equivalently for our case $\beta_{800nm} = 7.3 \times 10^{-30}$ esu. Finally, the value calculated in this way of d_{33} at 1064 nm is 6.9 pm V^{-1}, and at 800 nm it is 12.0 pm V^{-1}. At 118 °C, Folcia et al. reported a measured value of $d_{33} = 5.6$ pm V^{-1}, while our measurement at the same temperature gives $d_{33} = 14.9 \pm 2$ pm V^{-1}, highlighting the measurements presented here are consistent with those reported for a single temperature by Folcia et al. Altogether, this highlights the important dependence on wavelength for the second-order NLO susceptibilities of these materials in the 800–1200 nm range.

We repeat the same procedure for DIO, C1, and F7. The measured polarization and birefringence measurement data are shown in Figure S9 (Supporting Information). The polarization of C1 and F7 was determined via the standard triangular wave method, while the polarization data for DIO were taken from.[5] The molecular parameters of F7 were calculated as the weighted average of those of DIO and C1. The temperature dependence of the calculated coefficients for DIO, C1, and F7 is given in Figure 3, Figure 4, and Figure 5, respectively. Considering the simplicity of the model, the calculated values show a good agreement with the measured ones.

For the most accurate estimation of NLO coefficients, hyperpolarizability would need to be measured experimentally.[42] However, such measurements are delicate and time-consuming. With the increasing number of designed materials showing ferroelectric nematic and related phases, a thorough study of all to assess their potential for non-linear optics becomes an impractical task. Nevertheless, estimations obtained from DFT calculations show reasonably good agreement with experimental data. And while the full calculations are required for the most accurate estimation of the NLO properties, as polarization and order parameters of different FNLCs are usually on the same order of magnitude, a good indicator of high d_{33} is given by the value of the hyperpolarizability component β_{xxx}, as is evident from the Tables S1–S3 (Supporting Information).

4. Conclusion

We have determined the NLO susceptibility values of several relevant FNLC materials, which show a wide dispersion of values, highlighting that, in addition to a material exhibiting the ferroelectric nematic phase, the molecular design is of vital importance for its potential for non-linear optics implementation. Our measurements show that the highest NLO coefficient value is still held by the first FNLC, RM734. However, this material was not designed or intended to have optimal NLO properties; there is no reason that a molecule or a mixture with better NLO properties could not be synthesized in the future. With additional optimization by the addition of chromophores,[13] FNLCs could certainly surpass the NLO susceptibilities of the best solid-state NLO crystals.

A key challenge is then to be able to introduce effective π-bridged donor-acceptor groups with large electronic delocalization for maximizing NLO performance while at the same time preserving the molecular design requirements for retaining ferroelectric phases. Here, we have shown that molecular level hyperpolarizability calculations can be used for pre-screening the potentiality of new materials. In combination with computational approaches that are being developed for the design and prediction of polar order in new molecular architectures,[43] the presented approach can be used for assisted design of new materials with high NLO properties, accelerating the possibility of incorporating these new kind of polar materials into non-linear photonic applications.

The broader importance of these results is emphasized by the recent demonstration of nonlinear and electro-optic photonic devices based on FNLCs, including reconfigurable Pancharatman-Berry nonlinear diffractive optics,[44] nonlinear optical architectures based on FNLCs with geometric phase encoding,[45] Pockels effect based GHz-rate modulators integrating FNLCs into silicon photonics platforms,[46] and tunable photon-pair sources.[35] The quantitative values and temperature dependences reported here, provide the solid foundation for evaluating and developing such technologies. By giving both experimental benchmarks across different novel polar phases and guidance for material design, the present work should support and accelerate the integration of FNLCs into next-generation nonlinear-photonic platforms.

5. Experimental Section

Materials and Cells: Five liquid crystalline materials were investigated: RM734,[47] DIO,[5] FNLC-1571,[24] C1[26] and F7.[26] RM734, DIO and FNLC-1571 and their phase sequences (I-N-N_S-N_F-crystal) are reported elsewhere.[5,24,47,48] The novel compound C1 is a pure compound which has a phase sequence Iso – 225.6 °C – N – 154.3 °C – SmA – 129.7 °C – SmA_F – 90.1 °C – $SmC_P{}^H$. The material F7 is a mixture of 30% C1 and 70% DIO and has a phase sequence I – N – 97 °C – N_S — 86 °C – N_F – 10 °C – crystal. The materials RM734, DIO, C1, and F7 were synthesized according to the description given in references.[26,47,49] Structures of these materials are given in the Figure S1 (Supporting Information).

Two types of liquid crystal cells (assemblies in which liquid crystal material is sandwiched between two transparent substrates) were used. The first was the commercial wedge cells (KCRS-03, EHC) with surface coating rubbed parallel along the wedge and the wedge slope of $\alpha = 0.67°$. However, as some materials did not align well in these commercial cells, additional custom-made cells with a wedge slope α of 0.07° for DIO, and 0.057° and 1.27° for FNLC-1571. were prepared. These cells were composed of two indium tin oxide (ITO) coated glass plates, spin-coated with polyamide. Rubbing was applied in a parallel direction to the wedge. To create a wedge structure, spacers were placed only on one edge of the cell. The thickness of the cells was determined via spectral transmittance measurements (AvaSpec-2048, Avantes) and then additionally checked under the transmission microscope (Nikon Optiphot-2) using monochromatic light.

SHG Setup: The fundamental light source for SHG measurements was a pulsed Ti:Sapphire laser (Coherent Legend) generating 50 fs long pulses with a repetition rate of 1 kHz. The initial 50 fs long pulses with a spectral width FWHM = 22 nm were extended to 200 fs with the use of a Fabry-Pérot filter. The resulting beam had a central wavelength of 800 nm and a spectral width FWHM = 1.5 nm. A beam splitter was used to divert a part of the beam to a power meter (Coherent LabMax_TOP) to monitor the average power during the measurements.

After passing through a $\lambda/2$ waveplate and the polarizer, the collimated linearly polarized fundamental beam impinged on the sample as depicted in Figure 1. A 5x Nikon objective collected the generated second harmonic beam to a CMOS camera (BFS-U3-17S7M-C, Blackfly, Teledyne FLIR). The typical exposure time was ≈100 ms, the image size was 1600 × 1100 pixels, and the image resolution was 4.8 microns/pixel.

The temperature of the samples in commercial cells was controlled by an Instec HCS412W heating stage connected to an Instec mK2000 temperature controller. These cells have a wedge slope large enough that, within the laser beam spot size, multiple Maker fringes could be observed (Figure S7, Supporting Information). For the custom-made cells with a smaller slope, the use of a translation stage was required to move the cell along the wedge to obtain a suitable thickness difference. These samples were heated using the Instec HCS302XY heating stage mounted on a translation stage, and the temperature was controlled with an Instec mK2000B temperature controller.

To measure a specific component of the nonlinear susceptibility tensor d_{ij}, the orientation of the fundamental beam polarization and the analyzer for the second harmonic beam were set as shown in Figure 1. In those cases, for which no signal was obtained when using the Fabry-Pérot filter, which narrows the spectrum but reduces the optical power, the filter was removed from the optical path to increase the power. Without the filter, the spectrum of the fundamental beam exhibited quite a complex shape, as shown in Figure S4 (Supporting Information), which was also considered in the calculations.

The calibration of SHG measurements was performed by an NLO crystal sample, a Z-cut quartz. In this case, modification of the sample thickness and consequently Maker fringes were obtained by rotating the crystal plate around its vertical axis. A stepper motor rotation mount (K10CR1/M, Thorlabs) was used to control the rotation angle.

Maker Fringes Method: Since phase-matching could not be realized for any of the investigated materials, the nonlinear susceptibility tensor d_{ij} values could not be directly measured.[50] Instead, the values were determined using the standard Maker Fringes method. The optical power of the second harmonic beam oscillates with the thickness of the SHG active material L as:[51–54]

$$P_{2\omega} = \frac{S_{2\omega}\,\omega^2}{S_\omega^2 c_0^3 \epsilon_0}\,\frac{1}{n_{2\omega}^2}\,T d_{eff}^2\,P_\omega^2\,\frac{\sin^2\left(\frac{2\pi L}{\lambda}\Delta n_{ij}\right)}{\left(\frac{2\pi}{\lambda}\Delta n_{ij}\right)^2} \tag{9}$$

where S_ω and $S_{2\omega}$ are the cross-sectional areas of the fundamental and the SHG beam, ω is the fundamental beam frequency, c_0 the speed of light, ϵ_0 the vacuum permittivity, $n_{2\omega}$ the refractive index of the SHG active material at the frequency 2ω, T is the Fresnel transmission factor, d_{eff} is the effective nonlinear susceptibility (either d_{33}, d_{15} or d_{31} in our case), P_ω is the fundamental beam power, λ is the fundamental beam wavelength, and $\Delta\, n_{ij} = n_{i,2\omega} - n_{j,\omega}$ is the refractive index mismatch, where i/j refer either to the extraordinary or ordinary refractive index depending on the measurement geometry (Figure 1c,d). The setup-dependent constants can be replaced by the parameter α:

$$P_{2\omega} = \alpha\,\frac{1}{n_{2\omega}^2}\,T d_{eff}^2\,P_\omega^2\,\frac{\sin^2\left(\frac{2\pi L}{\lambda}\Delta n_{ij}\right)}{\Delta n_{ij}{}^2} \tag{10}$$

In order to obtain the d_{eff}, a 500 µm-thick Z-cut quartz plate was used as a reference. The SHG signal from the quartz plate was measured while rotating it around the crystallographic X-axis, thus effectively changing the length of the SHG active medium. Comparing the maximal intensities obtained from the measured sample $P_{2\omega}^m$ and the reference quartz plate $P_{2\omega}^{ref}$ the d_{eff} could be calculated as:

$$d_{eff} = d_{q,ref}\left(\frac{P_{2\omega}^m}{P_{2\omega}^{ref}}\,\frac{T^{ref}}{T^m}\right)^{\frac{1}{2}}\left(\frac{n_{2\omega}^m}{n_{2\omega}^{ref}} * \frac{\Delta n_{i,j}^m}{\Delta n^{ref}}\right) \tag{11}$$

The maximal intensities $P_{2\omega}^m$ were obtained by fitting. In the measurement without the Fabry-Pérot filter, the spectrum shown in Figure S4b (Supporting Information) was explicitly considered with the wavelength by a wavelength-weighted sum of signals, while the refractive index variation across the pulse wavelength dispersion was considered negligible. The optical parameters for quartz are well known, and their values are $d_{11} = 0.30 \pm 0.02$ pm V^{-1} and $\Delta n = 0.0194$.[12,55] For the calculation of the transmission factor of the liquid crystal cell T^m, all interfaces between air, glass, and liquid crystal were considered. The refractive index mismatch of the measured samples, $\Delta n_{i,j}^m$, was calculated from the period of the Maker fringes. The experimental uncertainties were accounted for by adopting a conservative 2% error in the cell slope reflecting the variations observed upon cooling/heating cycles, even though the slope can be measured with <0.1% precision in a single experiment. This slope error is propagated through the refractive index mismatch (Equation 10) and NLO-coefficient determinations (Equation 11). For the latter, the reported uncertainty of the quartz reference is also considered when calculating the final uncertainty range.

Birefringence and Refractive Index Measurement: Birefringence ($\Delta n = n_{e,2\omega} - n_{o,2\omega}$) of RM734, DIO, F7 and C1 for $\lambda = 405$ nm was measured by placing the wedge cell between crossed polarizers in the transmission polarizing optical microscope (POM) using monochromatic light and analyzing transmitted intensity as a function of thickness (Figure S10, Supporting Information), where $I = I_0 \sin^2(\pi \Delta n L/\lambda)$. To assess the accuracy of the measurements of the refractive index mismatch (Δn_{ij}) determined from NLO measurements, we compared the measured birefringence Δn of RM734 with the $n_{e,2\omega} - n_{2o,\omega}$ value that can be calculated from the three Δn_{ij} terms, namely $n_{e,2\omega} - n_{e,\omega}$, $n_{o,2\omega} - 0.5(n_{o,\omega} + n_{e,\omega})$ and $n_{e,2\omega} - n_{o,\omega}$ obtained from Maker's fringes experiments. The difference between both values was found to be below 2%, confirming the reliability of the NLO-derived refractive index mismatch measurements.

Finally, the refractive indices were measured by the optical interference method.[56] The wedge cell was observed under a microscope in reflection mode with an optical filter $\lambda = 405$ nm. To determine n_e and n_o, incoming light was polarized along and perpendicular to the director, respectively. The values of the refractive index were calculated from the period of the interference fringes and are summarized in Table S4 (Supporting Information).

Supporting Information

Supporting Information is available from the Wiley Online Library or from the author.

Acknowledgements

The authors thank Janja Milivojević for carrying out the fabrication of the custom-made liquid crystal cells. The ferroelectric nematic liquid crystal

FNLC-1571 used in this work was supplied by Merck Electronics KGaA. M.L., L.C., A.M, I.D.O., and N.S. acknowledge the support of the Slovenian Research Agency (Grant Nos. P1-0192, J1-50004, PR-11214-1, and BI-VB/25-27-011). C.J.G., J.H., and R.J.M. acknowledge funding from UKRI via a Future Leaders Fellowship, grant No. MR/W006391/1.

Conflict of Interest

The authors declare no conflict of interest.

Data Availability Statement

The data that support the findings of this study are openly available in Zenodo at https://doi.org/10.5281/zenodo.17983956.

Keywords

ferroelectric nematic fluid, maker fringes method, NLO susceptibility

Received: September 12, 2025
Revised: November 20, 2025
Published online:

[1] R. Dorn, D. Baums, P. Kersten, R. Regener, *Adv. Mater.* **1992**, *4*, 464.
[2] F. De Martini, F. Sciarrino, *Prog. Quantum Electron.* **2005**, *29*, 165.
[3] M. M. Fejer, *Phys. Today* **1994**, *47*, 25.
[4] J. V. Moloney, *Nonlinear Optical Materials*, Springer, New York, NY, **1998**.
[5] H. Nishikawa, K. Shiroshita, H. Higuchi, Y. Okumura, Y. Haseba, S. Yamamoto, K. Sago, H. Kikuchi, *Adv. Mater.* **2017**, *29*, 1702354.
[6] R. J. Mandle, S. J. Cowling, J. W. Goodby, *Phys. Chem. Chem. Phys.* **2017**, *19*, 11429.
[7] N. Sebastián, L. Cmok, R. J. Mandle, M. R. de la Fuente, I. Drevenšek Olenik, M. Čopič, A. Mertelj, *Phys. Rev. Lett.* **2020**, *124*, 037801.
[8] X. Chen, E. Korblova, D. Dong, X. Wei, R. Shao, L. Radzihovsky, M. A. Glaser, J. E. Maclennan, D. Bedrov, D. M. Walba, N. A. Clark, *Proc. Natl. Acad. Sci. USA* **2020**, *117*, 14021.
[9] N. Sebastián, M. Čopič, A. Mertelj, *Phys. Rev. E* **2022**, *106*, 021001.
[10] C. L. Folcia, J. Ortega, R. Vidal, T. Sierra, J. Etxebarria, *Liq. Crys.* **2022**, *49*, 899.
[11] R. Xia, X. Zhao, J. Li, H. Lei, Y. Song, W. Peng, X. Zhang, S. Aya, M. Huang, *J. Mater. Chem. C* **2023**, *11*, 10905.
[12] I. Shoji, T. Kondo, A. Kitamoto, M. Shirane, R. Ito, *J. Opt. Soc. Am. B* **1997**, *14*, 2268.
[13] J. Ortega, C. L. Folcia, T. Sierra, *Liq. Cryst.* **2025**, *52*, 801.
[14] H. Nishikawa, F. Araoka, *Adv. Mater.* **2021**, *33*, 2101305.
[15] X. Zhao, J. Zhou, J. Li, J. Kougo, Z. Wan, M. Huang, S. Aya, *Proc. Natl. Acad. Sci. USA* **2021**, *118*, 2111101118.
[16] C. Feng, R. Saha, E. Korblova, D. Walba, S. N. Sprunt, A. Jákli, *Adv. Opt. Mater.* **2021**, *9*, 2101230.
[17] X. Zhao, H. Long, H. Xu, J. Kougo, R. Xia, J. Li, M. Huang, S. Aya, *Proc. Natl. Acad. Sci. USA* **2022**, *119*, 2205636119.
[18] X. Zhao, J. Li, M. Huang, S. Aya, *J. Mater. Chem. C* **2023**, *11*, 8547.
[19] N. Sebastián, M. Lovšin, B. Berteloot, N. Osterman, A. Petelin, R. J. Mandle, S. Aya, M. Huang, I. Drevenšek-Olenik, K. Neyts, A. Mertelj, *Nat. Commun.* **2023**, *14*, 3029.
[20] X. Chen, E. Korblova, M. A. Glaser, J. E. Maclennan, D. M. Walba, N. A. Clark, *Proc. Natl. Acad. Sci. USA* **2021**, *118*, 2104092118.
[21] Y.-T. Hsiao, I. Nys, K. Neyts, *Soft Matter* **2023**, *19*, 8617.
[22] H. Kamifuji, K. Nakajima, M. Nakase, Y. Tsukamoto, M. Ozaki, H. Kikuchi, *Appl. Phys. Express* **2025**, *18*, 045502.
[23] H. Kamifuji, K. Nakajima, Y. Tsukamoto, M. Ozaki, H. Kikuchi, *Appl. Phys. Express* **2023**, *16*, 071003.
[24] M. Lovšin, A. Petelin, B. Berteloot, N. Osterman, S. Aya, M. Huang, I. Drevenšek-Olenik, R. J. Mandle, K. Neyts, A. Mertelj, N. Sebastian, *Giant* **2024**, *19*, 100315.
[25] N. Sebastián, R. J. Mandle, A. Petelin, A. Eremin, A. Mertelj, *Liq. Cryst.* **2021**, *48*, 2055.
[26] C. J. Gibb, J. Hobbs, D. I. Nikolova, T. Raistrick, S. R. Berrow, A. Mertelj, N. Osterman, N. Sebastián, H. F. Gleeson, R. J. Mandle, *Nat. Commun.* **2024**, *15*, 5845.
[27] A. Erkoreka, M. Huang, S. Aya, J. Martinez-Perdiguero, *Phys. Rev. Lett.* **2024**, *133*, 208101.
[28] H. Kikuchi, H. Matsukizono, K. Iwamatsu, S. Endo, S. Anan, Y. Okumura, *Adv. Sci.* **2022**, *9*, 2202048.
[29] J. Karcz, J. Herman, N. Rychłowicz, P. Kula, E. Górecka, J. Szydlowska, P. W. Majewski, D. Pociecha, *Science* **2024**, *384*, 1096.
[30] G. J. Strachan, E. Górecka, D. Pociecha, *Mater. Horiz.* **2025**.
[31] H. Nishikawa, D. Okada, D. Kwaria, A. Nihonyanagi, M. Kuwayama, M. Hoshino, F. Araoka, *Adv. Sci.* **2024**, *11*, 2405718.
[32] D. Pociecha, R. Walker, E. Cruickshank, J. Szydlowska, P. Rybak, A. Makal, J. Matraszek, J. M. Wolska, J. M. D. Storey, C. T. Imrie, E. Gorecka, *J. Mol. Liq.* **2022**, *361*, 119532.
[33] D. Pociecha, J. Szydlowska, N. Vaupotič, K. Kwiatkowska, M. Juodka, J. Spiess, J. M. Storey, C. T. Imrie, R. Walker, E. Gorecka, *Adv. Sci.* **2025**, *12*, 08405.
[34] X. Chen, V. Martinez, E. Korblova, G. Freychet, M. Zhernenkov, M. A. Glaser, C. Wang, C. Zhu, L. Radzihovsky, J. E. Maclennan, D. M. Walba, N. A. Clark, *Proc. Natl. Acad. Sci. USA* **2023**, *120*, 2217150120.
[35] V. Sultanov, A. Kavčič, E. Kokkinakis, N. Sebastián, M. V. Chekhova, M. Humar, *Nature* **2024**, *631*, 294.
[36] D. A. Dunmur, *Chem. Phys. Lett.* **1971**, *10*, 49.
[37] A. A. Minko, V. S. Rachkevich, S. Ye. Yakovenko, *Liq. Cryst.* **1989**, *4*, 1.
[38] P. Palffy-Muhoray, D. A. Balzarini, *Can. J. Phys.* **1981**, *59*, 515.
[39] A. Erkoreka, N. Sebastián, A. Mertelj, J. Martinez-Perdiguero, *J. Mol. Liq.* **2024**, *407*, 125188.
[40] P. Günter, *Nonlinear Optical Effects and Materials*, Springer, Berlin, Heidelberg, **2000**.
[41] L. T. Cheng, W. Tam, S. H. Stevenson, G. R. Meredith, G. Rikken, S. R. Marder, *J. Phys. Chem.* **1991**, *95*, 10631.
[42] F. Araoka, B. Park, Y. Kinoshita, H. Takezoe, J. Thisayukta, J. Watanabe, *Mol. Crys. Liq. Crys.* **1999**, *328*, 291.
[43] J. Hobbs, C. J. Gibb, R. J. Mandle, *J. Mater. Chem. C* **2025**, *13*, 13367.
[44] H.-F. Chen, X.-Y. Tao, B.-H. Zhu, J.-T. Pan, L.-L. Ma, C. Chen, W.-G. Zhu, W. Chen, Y.-Q. Lu, *Light Sci Appl* **2025**, *14*, 314.
[45] J.-T. Pan, B.-H. Zhu, L.-L. Ma, W. Chen, G.-Y. Zhang, J. Tang, Y. Liu, Y. Wei, C. Zhang, Z.-H. Zhu, W.-G. Zhu, G. Li, Y.-Q. Lu, N. A. Clark, *Nat. Commun.* **2024**, *15*, 8732.
[46] I. Taghavi, O. Esmaeeli, S. J. Chowdhury, K. M. Awan, M. Hammood, M. Mitchell, D. Witt, C. Pecinovsky, J. Sickler, J. F. Young, N. A. F. Jaeger, S. Shekhar, L. Chrostowski, *Nat. Commun.* **2025**, *16*, 8902.
[47] R. J. Mandle, S. J. Cowling, J. W. Goodby, *Chem. – A Eur. J.* **2017**, *23*, 14554.
[48] J. Thoen, G. Cordoyiannis, W. Jiang, G. H. Mehl, C. Glorieux, *Phys. Rev. E* **2023**, *107*, 014701.
[49] J. Li, H. Nishikawa, J. Kougo, J. Zhou, S. Dai, W. Tang, X. Zhao, Y. Hisai, M. Huang, S. Aya, *Sci. Adv.* **2021**, *7*, abf5047.

[50] G. E. Francois, *Phys. Rev.* **1966**, *143*, 597.
[51] J. Jerphagnon, S. K. Kurtz, *J. Appl. Phys.* **1970**, *41*, 1667.
[52] A. Majkić, A. Franke, R. Kirste, R. Schlesser, R. Collazo, Z. Sitar, M. Zgonik, *Phys. Status Solidi B* **2017**, *254*, 1700077.
[53] W. N. Herman, L. M. Hayden, *J. Opt. Soc. Am. B* **1995**, *12*, 416.
[54] P. D. Maker, R. W. Terhune, M. Nisenoff, C. M. Savage, *Phys. Rev. Lett.* **1962**, *8*, 21.
[55] P. Kaatz, D. P. Shelton, *J. Chem. Phys.* **1996**, *105*, 3918.
[56] P. Kumari, B. Basnet, M. O. Lavrentovich, O. D. Lavrentovich, *Science* **2024**, *383*, 1364.